Sustainable Sulfur-Carbon Hybrids for Efficient Sulfur Redox Conversions in Nanoconfined Spaces

Senokos, Evgeny; Au, Heather; Eren, Enis Oğuzhan; Horner, Tim; Song, Zihan; Tarakina, Nadezda V.; Yılmaz, Elif Begüm; Vasileiadis, Alexandros; Giusto, Paolo; More Authors

DOI
10.1002/smll.202407300

Publication date
2024

Document Version
Final published version

Published in
Small

NANO · MICRO small
www.small-journal.com

Sustainable Sulfur-Carbon Hybrids for Efficient Sulfur Redox Conversions in Nanoconfined Spaces

Evgeny Senokos, Heather Au, Enis Oğuzhan Eren, Tim Horner, Zihan Song, Nadezda V. Tarakina, Elif Begüm Yılmaz, Alexandros Vasileiadis, Hannes Zschiesche, Markus Antonietti, and Paolo Giusto**

Nanoconfinement is a promising strategy in chemistry enabling increased reaction rates, enhanced selectivity, and stabilized reactive species. Sulfur's abundance and highly reversible two-electron transfer mechanism have fueled research on sulfur-based electrochemical energy storage. However, the formation of soluble polysulfides, poor reaction kinetics, and low sulfur utilization are current bottlenecks for broader practical application. Herein, a novel strategy is proposed to confine sulfur species in a nanostructured hybrid sulfur-carbon material. A microporous sulfur-rich carbon is produced from sustainable natural precursors via inverse vulcanization and condensation. The material exhibits a unique structure with sulfur anchored to the conductive carbon matrix and physically confined in ultra-micropores. The structure promotes Na^+ ion transport through micropores and electron transport through the carbon matrix, while effectively immobilizing sulfur species in the nanoconfined environment, fostering a quasi-solid-state redox reaction with sodium. This translates to ≈99% utilization of the $2e^-$ reduction of sulfur and the highest reported capacity for a room temperature Na^-S electrochemical system, with high rate capability, coulombic efficiency, and long-term stability. This study offers an innovative approach toward understanding the key physicochemical properties of sulfurcarbon nanohybrid materials, enabling the development of high-performance cathode materials for room-temperature Na-S batteries with efficient sulfur utilization.

1. Introduction

The growing attention toward nanocompartmented matter is attributed to the greatly different set of properties of chemical species in (sub)nanometer confined spaces. Living organisms, such as biological cells, have exploited the properties of nanoconfined species for a long to preserve proteins against oxidation and promote chemical/enzymatic reactions under mild conditions with excellent selectivity.[1] The recent advancements in the field of nanotechnology have inspired scientists to develop diverse nanoconfined systems, aiming to mimic natural biological processes and achieve enhanced selectivity for efficient chemical reactions and remarkable acceleration in reaction rates.[2,3]

Nanoconfinement alters the chemical and physical properties of the confined species[4] and has a strong impact on the chemical reactions from both thermodynamic and kinetics aspects.[1,5] The steric limitations imposed by nanoconfinement restrict the size and shape of the resulting products, thereby amplifying or modifying the selectivity toward products.[6–8] Furthermore, the size confinement provides an increased local concentration of the reagents that can accelerate chemical reactions, while hindering the diffusion of unwanted external species (such as a solvent), thereby providing a "protected" environment.[9,10]

Subnanometer pores of nanomaterials can be used as "molecular vessels" partially encapsulating and thus stabilizing metastable species.[11,12] This was found to be an effective

E. Senokos, E. O. Eren, T. Horner, Z. Song, N. V. Tarakina, E. B. Yılmaz, H. Zschiesche, M. Antonietti, P. Giusto
Department of Colloid Chemistry
Max Planck Institute of Colloids and Interfaces
14476 Potsdam, Germany
E-mail: evgeny.senokos@mpikg.mpg.de; paolo.giusto@mpikg.mpg.de

The ORCID identification number(s) for the author(s) of this article can be found under https://doi.org/10.1002/smll.202407300

DOI: 10.1002/smll.202407300

H. Au
Department of Chemical Engineering
Imperial College London
London SW7 2AZ, UK

A. Vasileiadis
Storage of Electrochemical Energy
Department of Radiation Science and Technology
Faculty of Applied Sciences
Delft University of Technology
Delft 2629JB, The Netherlands

strategy for highly reactive electrochemical systems in catalysis and energy storage.[13–15] In particular, the confinement of sulfur species has a paramount impact on electrochemical systems based on sulfur conversion reactions. For example, the high reactivity of sulfur species with metal ions and the high solubility of polysulfide intermediates, among the primary causes of device failure, can be tackled by physical encapsulation of sulfur in nanocavities. If the sulfur nanophases can be accessed by metal ions and electrons through a nanopore network, while larger sulfide or polysulfide species are hindered from exiting the pores, the reaction occurs practically in a quasi-solid-state, at rates potentially only restricted by the slowest transport mechanism, which is nevertheless rather fast transport of metal ions. This in return is expected to enhance the stability and kinetics of sulfur conversion as well as the degree of sulfur utilization for the two-electron process. However, despite several strategies being adopted to confine sulfur clusters within nanospaces, including chemical anchoring and physical confinement, quantitative reversible exploitation was far from being truly accomplished.[14,16–18]

The common approach for the isolation of sulfur in a restricted space is based on designing host materials with a preorganised porous matrix which is subsequently infiltrated with sulfur in a fluid state.[19–21] This infers that sulfur can access and infiltrate open pores, which automatically sets a pathway for a reverse loss of the active material through the same loading channels. Furthermore, a considerable portion of the added sulfur remains not electronically connected and thereby inactive, as reflected in substoichiometric utilization. Therefore, we intend to develop a novel synthetic method where a conductive, microporous carbon is formed around a sulfur nanophase, which after synthesis is then entrapped in a too-small-to-move micropore system. Such a confined nanosulfur@microporous carbon nanophase also prevents the diffusion of solvent molecules and is thereby effectively a solid-state cathode material, providing a promising avenue for addressing several concomitant issues including sulfur leakage, sluggish reaction kinetics, volume expansion, and quantitative availability and exploitation.

Herein, we report on a one-step strategy to obtain a hybrid sulfur-carbon (SC) material via inverse vulcanization of elemental sulfur and linalool, in situ thermally polymerized and thermally condensed. The thermal treatment enables the formation of a conductive carbon framework around the sulfur species that encapsulates and stabilizes sulfur at these temperatures. The confined sulfur chains are uniformly distributed all over the material within carbon nanocavities with subnanometer size. By controlling the precursor's chemistry and the relative sulfur ratio we can tune the morphology and chemical composition of the sulfur-carbon material to achieve the desired confinement and quantitative utilization of sulfur. A major advantage of the hybrid carbon matrix with confined sulfur is demonstrated by the reversible electrochemical conversion of elemental sulfur to Na_2S. In this way, it can achieve ≈100% sulfur utilization, retaining a high reaction rate even after 1500 cycles. This work provides a facile and sustainable strategy toward the synthesis of hybrid carbon matrices with nanoconfined elemental sulfur, with potential high-interest applications in catalysis and electrochemical energy storage.

2. Results and Discussion

2.1. One-Pot Inverse Vulcanization-Thermal Condensation of Sulfur and Linalool

Inspired by the evolution of natural biological systems, in which the protecting shell is built around living organisms, this work aims to produce a hybrid sulfur carbon structure with sulfur species confined within the carbon matrix during materials formation. For this purpose, sulfur-carbon materials were synthesized by a one-pot process summarised in **Figure 1a**. The mixture of sulfur and linalool was heated to 175 °C triggering the free radical ring-opening of S_8, reacting at the vinylic bonds of linalool. The reaction continues with the propagation of the polymer until all available sulfur and/or dienes are consumed, leading to a network of linear sulfur units cross-linked by linalool. To control the contribution of sulfur bridges in the copolymer, the mass ratio between S_8 and linalool (S:Lin) was varied from 50:50 to 90:10. ^{1}H NMR spectra (Figure S2, Supporting Information) showed a gradual fading of the signals related to the alkene protons located between 5 and 6 ppm upon increase of the sulfur content in the precursor mixture. The full disappearance of the signals at the S:Lin ratio of 90:10 suggests that all double bonds successfully reacted with sulfur radicals. Gel permeation chromatography (GPC) revealed a relatively low average molecular weight of the sulfur copolymer around M_w = 1300 g mol^{-1}, which does not significantly change by varying the S:Lin ratio in the precursor mixture.

After completion of the inverse vulcanization, the sulfur copolymers were directly subjected to a thermal condensation step in the N_2 atmosphere at 800 °C. During heating, the polymers exhibit a major weight loss at ≈210 °C due to the cleavage of the S—S bonds (Figure S3, Supporting Information) and the sublimation of a fraction of the sulfur. Further heating at elevated temperatures leads to a gradual increase of carbon–carbon condensates, where carbon arranges into stacked conjugated pseudo graphitic domains until the remaining reactive sulfur is encapsulated and thereby stabilized. As expected, the yield of the SC after the thermal condensation is inversely correlated with the S:Lin ratio in the precursor.

2.2. Morphology and Structural Characteristics

The morphology and structure of the resulting SCs significantly change with an increase in the sulfur content in the precursor mixture (**Figure 2a**). Scanning electron microscopy (SEM) images of the 50:50 and 70:30 samples reveal an irregular morphology composed of large chunks with rough surfaces and sharp edges. A further increase in the S:Lin precursor mixture ratio to 80:20 and 90:10 causes a drastic change in the morphology of the SC from alarge chunks to spherical-like nanoparticles with an average size in the range of 50–150 nm. At the nanoscale (Figure 2c), the primary nanoparticles of the S:Lin 80:20 sample are aggregated into large clusters, in contrast to the micrometre-scale rectangular flakes observed for S:Lin 50:50 (Figure 2b). High-resolution transmission electron microscopy (HR-TEM) images show that the sulfur carbons have a turbostratic nanostructure with graphitic domains distributed in an amorphous

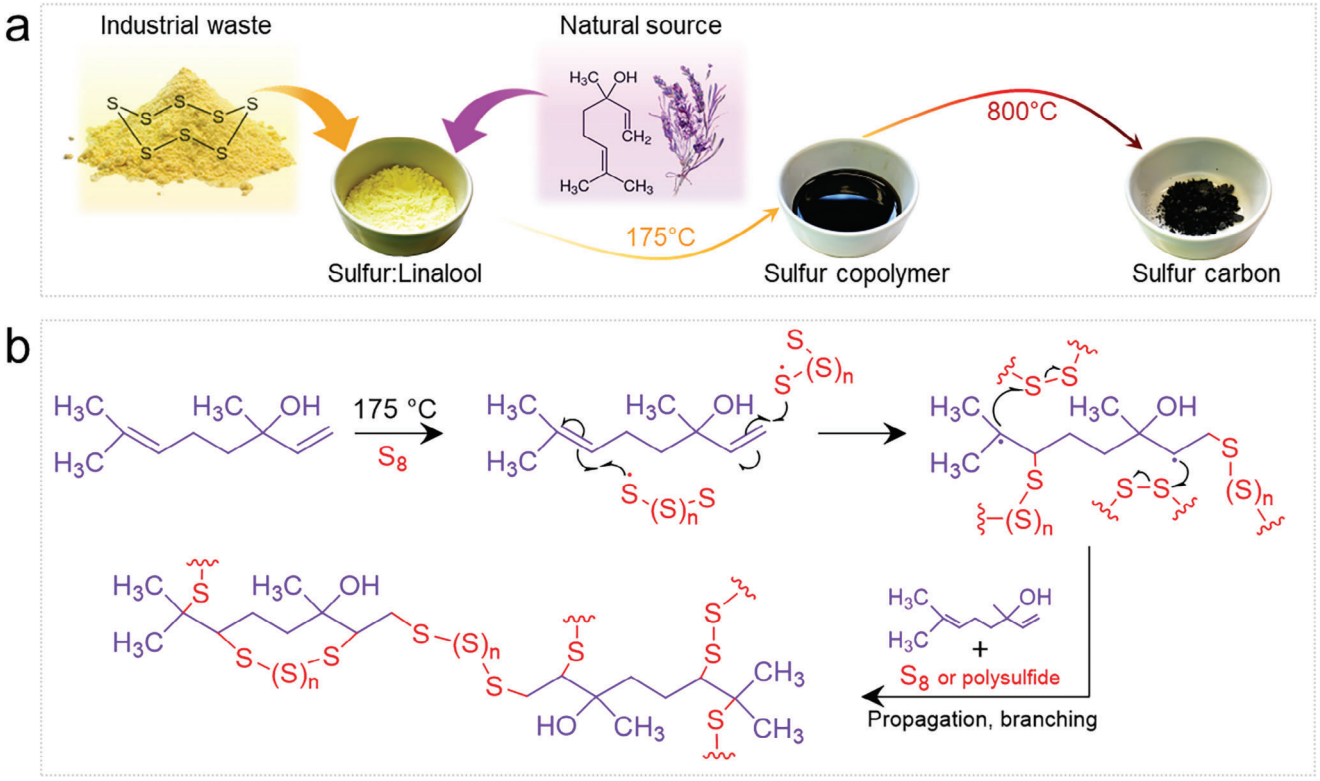

Figure 1. a) Schematic diagram illustrating the synthesis of sulfur carbon composite material and b) scheme of the inverse vulcanization reaction of elemental sulfur and linalool.

carbon matrix, typical of hard carbons. The interlayer distance estimated from TEM fringe analysis (Figure S4, Supporting Information) is in the range of 0.35-0.39 nm, larger than that of graphite (0.33 nm),[22] which can be ascribed to the introduction of the larger S atoms within the carbon matrix.[23] The average distance between the graphitic-like planes was found to be in the same range for all the samples. However, HRTEM images reveal a higher degree of order, with longer and more aligned stacks of the layers for sulfur carbons obtained at larger S:Lin ratios (Figure S4, Supporting Information). This points to the fact that the excess sulfur indeed acts as a high-temperature solvent to optimize carbon-carbon reconnection, and the more sulfur present, the longer the carbon phase extends.

The similarity of microstructure between the samples was also confirmed by X-ray diffraction (XRD) and Raman spectroscopy. The two broad peaks at 22.8° and 42.8° observed in XRD are attributed to the (002) and (100) crystal planes in carbon materials (Figure S5a, Supporting Information).[24–26] The average interlayer spacing (d_{002}) estimated by Bragg's law is 0.39 nm for all materials, in good agreement with TEM observations. Furthermore, the increased degree of order in the material prepared at higher sulfur content is consistent with a more intense and sharper (002) X-ray diffraction peak. The intensity ratio of the D band at ≈1350 cm^{-1} to the sp^2 vibrational G band at ≈1580 cm^{-1} in the Raman spectra is ≈0.97 for all sulfur loadings, similar to that of typical hard carbons (Figure S5b, Supporting Information).[25,26] The appearance of a pronounced peak at 372 cm^{-1} can be assigned to the C—S bond stretching.[27–29] At the same time, the absence of the strong Raman signal below 500 cm^{-1} associated with S—S vibrational modes can be attributed to the phonon confinement effect, previously observed for carbon-sulfur nanocomposites.[30,31]

Open porosity and the available surface of the materials were investigated by CO_2 and N_2 sorption analyses, revealing a predominantly microporous structure (Figure S6 and Table S1, Supporting Information). Specific surface area (SSA) obtained from CO_2 adsorption curves gradually decreases from 936 to 629 $m^2\ g^{-1}$ with higher sulfur content. Non-local density functional theory (NLDFT) analysis indicates that most of the pores accessible to CO_2 are in the range of ultra-micropores, between 0.3 and 0.7 nm (Figure S6b, Supporting Information). Such a narrow range of pore diameters is optimal for suppressing the shuttle effect of soluble polysulfides[20,32] and, since the size of the pores is smaller than the size of the solvated Na^+ ions (but bigger than the non-solvated Na^+), the ideal for achieving a quasi-solid-state reaction mechanism.[33]

Energy-dispersive spectroscopy (EDS) mapping indicates a uniform distribution of C, O, and S throughout the samples (Figure 2d; Figure S7, Supporting Information). The sulfur content in the SCs, obtained by means of combustive elemental analysis (EA), exhibits a gradual increase from 16.6 to 20 wt.%, with increasing S:Lin ratio in the precursor mixture (Table S2, Supporting Information).

X-ray photoelectron spectra (XPS) (Figure 2e) confirm a pronounced increase in sulfur content for the S:Lin 80:20 and 90:10 SCs in good agreement with EA results. The four characteristic peaks located at 164, 228, 285, and 534 eV correspond to the S2p, S2s, C1s, and O1s, respectively.[34] The high-resolution

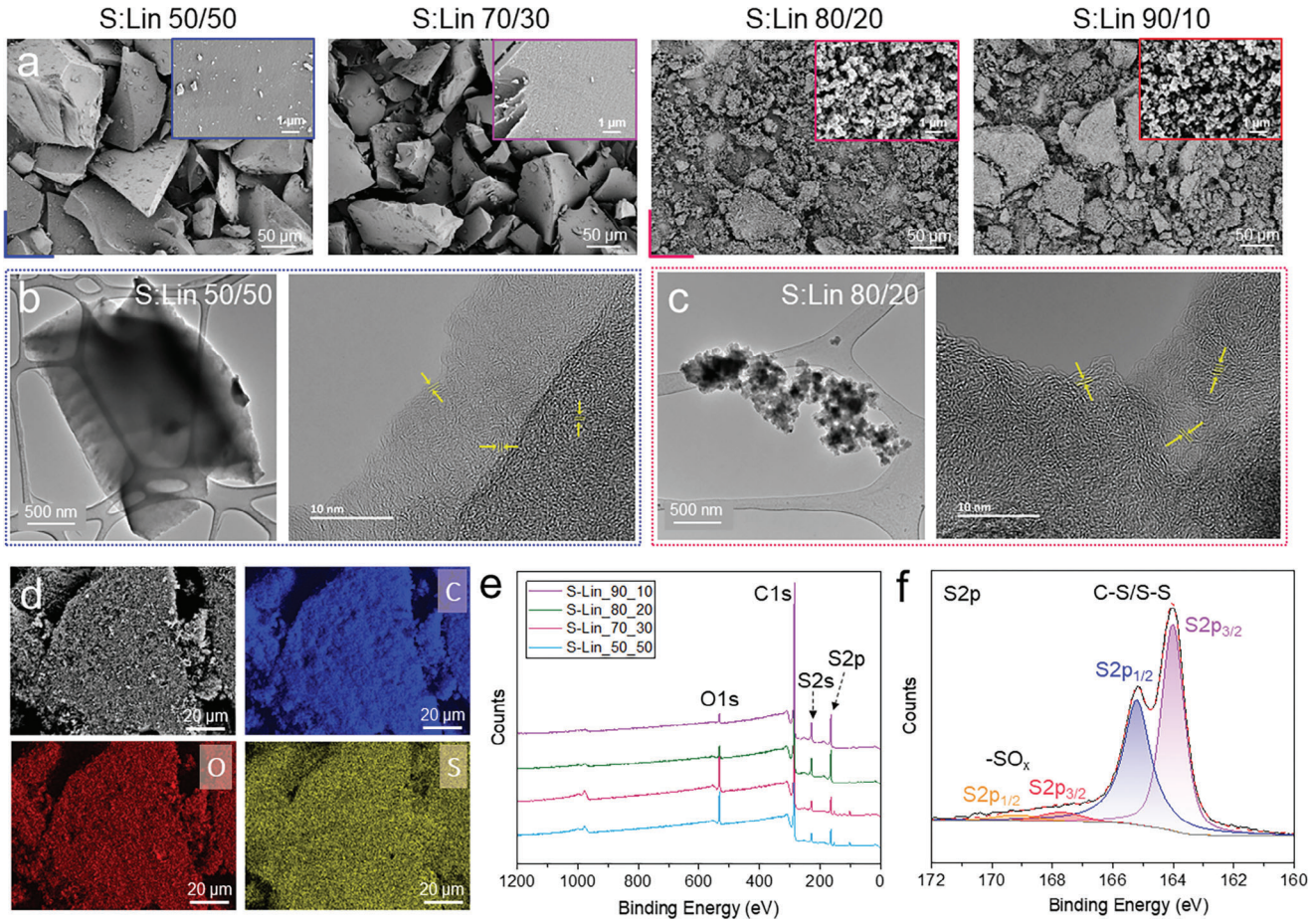

Figure 2. a) SEM images of sulfur carbon composite material at different sulfur to linalool ratios in the precursor mixture and HRTEM images of b) S:Lin 50/50 and c) S:Lin 80/20 samples; d) EDS mapping of S:Lin 90/10, e) XPS survey spectra of the sulfur carbons at different S:Lin ratio and f) high-resolution S2p XPS spectra for S:Lin 90/10.

S2p spectrum of the peak is deconvoluted into two components (Figure 2f; Figure S8, Supporting Information). The low binding energy doublet at 164.0 eV ($S2p_{3/2}$) and 165.2 eV ($S2_{p1/2}$) is attributed to covalent C—S bonds or S—S bonds of the nanoconfined sulfur chains.[34,35] The binding energies of S2p for C—S and S—$(S)_x$—S species are very close to that of elemental sulfur,[36] making it difficult to unequivocally assign these peaks to either one of these chemical groups. The higher binding energy peaks at 167.8 and 169.2 eV are attributed to oxidized sulfur —C—SO_x groups, minorly contributing to the overall structure. Therefore, the evolution of the chemical state of sulfur was studied by a combination of physico-chemical techniques and electrochemical methods. The presence of free elemental sulfur (S_8) in the S:Lin materials is excluded by thermogravimetric analysis (TGA) showing no significant mass loss between 180 and 360 °C, which is a characteristic range for sublimation of sulfur (Figure S9, Supporting Information).[37]

Deconvolution of the C1s XPS spectra displays a dominant contribution from sp^2-C/sp^3-C at 284.7 eV, along with other features associated with C—S at 285.4 eV, C—O/C═O at 286.6 eV, and —O—C═O at 288.7 eV (Figure S8b, Supporting Information). The increase of the S:Lin ratio is reflected in minor changes of the relative ratios between —C—SO_x and C—S peaks in the S2p core-level and between sp^2/sp^3 C—C, C—S carbon and oxygen—carbon bonds in the C1s peak.

In addition, electron energy loss spectra (EELS) reveal similar chemical structures of the SCs at different S:Lin ratios at the nanoscale (Figure S10, Supporting Information). The shape of the carbon K-edge spectra resembles the typical shape of hard carbon materials. The spectra exhibit no significant peak shift or additional features between the samples with different S:Lin ratios (Figure S10a, Supporting Information). A negligible change in the relative intensity was observed for the 1s → π^* signal at 284 eV (C═C) and a broad 1s → σ^* feature > 291 eV (C—C), confirming a similar sp^2 to sp^3 carbon ratio. Similarly, minor differences were observed in relatively weak sulfur L-edge signal (Figure S10b, Supporting Information).

2.3. Quantitative Confinement for High Sulfur Utilization

To explore the effect of sulfur encapsulation in ultra-micropores of the carbon on the stability and activity of the sulfur species, electrochemical multistep conversion of S^0 to Na_2S was investigated. The irreversible shuttling of metal polysulfide species

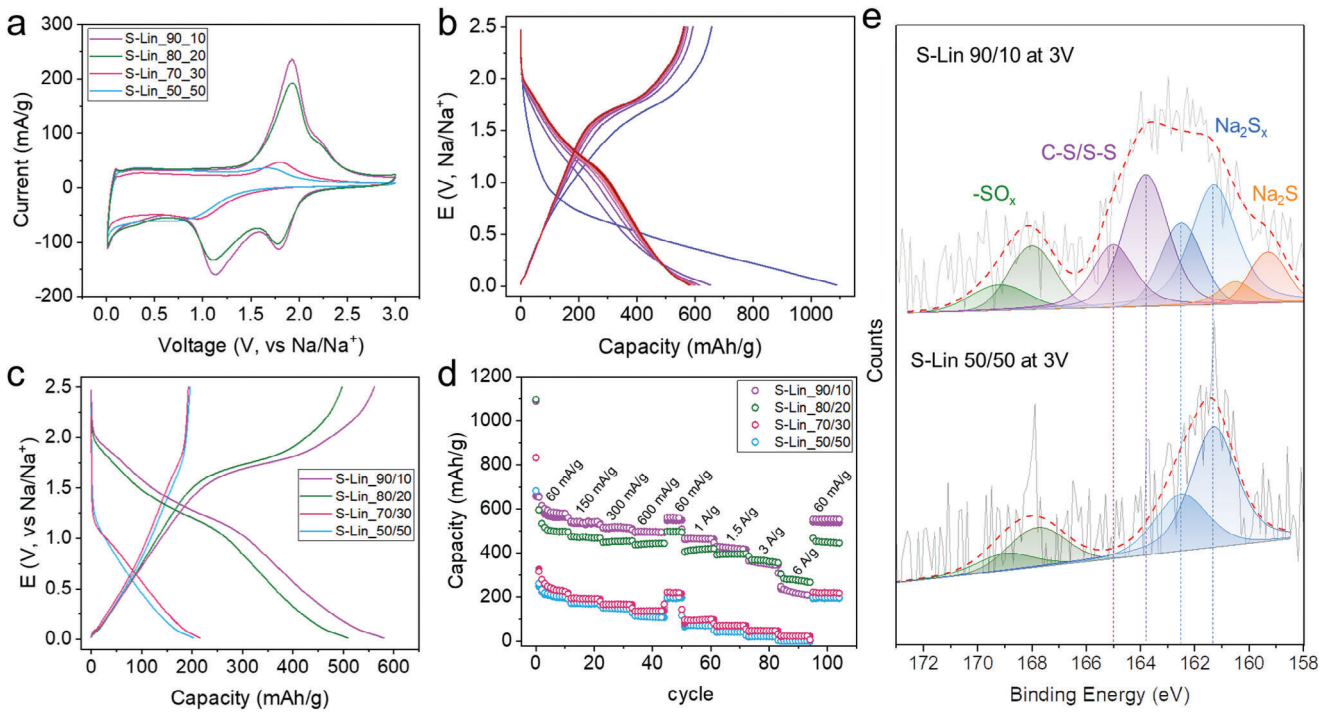

Figure 3. Electrochemical performances of the four sulfur carbon samples (vs Na/Na^+). a) CV at 0.1 mV s^{-1} within a potential window of 0.01–3.0 V, b) activation of sulfur in S:Lin 90/10 800 °C electrode during first ten galvanostatic cycles at 60 mA g^{-1}, c) the 10th galvanostatic charge/discharge profiles at 60 mA g^{-1} and d) rate performance at different current densities of the SC electrodes at different S:Lin ratio; e) ex situ S2p XPS spectra of S:Lin 50/50 and S:Lin 90/10 electrodes charged to 3.0 V.

widely explored for electrochemical systems based on Li—S couple is significantly exacerbated for Na-S due to the more reactive nature of sodium.[38,39] This greatly restricts a broad application of the sustainable reaction between sulfur and sodium for the electrochemical storage of energy and makes it an interesting model system for this study.

The effect of the sulfur:linalool ratio during inverse vulcanization on the electrochemical behavior of the SC composite materials was investigated in electrochemical cells against a sodium electrode at room temperature. During the first reaction cycle (Figure S11, Supporting Information), a sharp irreversible cathodic peak is observed for all the samples at < 0.5 V (vs Na^+/Na), related to the decomposition of the electrolyte solution causing the formation of the solid–electrolyte interphase (SEI) layer, and irreversible insertion of Na^+ into the carbon structure.[40,41] It is worth noticing that no indication of redox processes related to sulfur conversion reaction, typically observed between 1.0 and 2.5 V (vs Na^+/Na) is noticed. Instead, initial cycles act as an activation step after which the Faradaic processes, reflected in pronounced redox peaks (Figure S11, Supporting Information), start arising. This points to hindered access to the sulfur species confined in ultra-micropores between stacked carbon layers.[42,43]

Figure 3a presents cyclic voltammetry (CV) cycles for the sulfur carbon samples at a scan rate of 0.1 mV s^{-1}. Upon subsequent cycles for the S:Lin 50/50 and S:Lin 70/30, a pair of redox peaks emerge at 0.9 V/1.7 V, attributed to the solid-solid transition between the insoluble Na_2S_2 and Na_2S, typically observed at a low potential range.[44] In this case, the electrochemical cleavage of C—S and short-chain S—S bonds during initial sodiation causes the irreversible formation of Na_2S_2.

With the increase of the sulfur content to S:Lin 80/20 and further to S:Lin 90/10, two pairs of redox peaks appear at 1.1/1.9 V and 1.7/2.2 V (Figure 3a), which resembles the previously reported behavior of sulfur cathodes in Na-S batteries.[32,45,46] These peaks correspond to a two-step reaction, where sulfur species first form sodium polysulfide intermediates via a $2Na^+/2e^-$ process at ≈1.8 V versus Na/Na^+, and subsequently convert to Na_2S at ≈1.2 V.[47–49] At higher scan rates, a slight shift of the redox peaks is observed, while the capacity remains reversible upon cycling (Figure S12a, Supporting Information).

To gain more insight into the kinetics of the electrochemical processes, the diffusion coefficient (D_{Na^+}) was estimated by the Randles–Sevcik equation (see Figure S12, Supporting Information). The D_{Na+} value is $5.2 \cdot 10^{-8}$ cm^2 s^{-1}, which is significantly larger than that of previously reported sulfur-based materials (10^{-10}–10^{-14}),[50–54] depicting an outstanding high ionic diffusion rate and reactivity of sulfur in the material, pointing to a tight nanoconfinement in the structural pores.

A double logarithmic plot of the peak current density (i) versus scan rate (v): $\lg(i) = b \log(v) + \log(k)$, (Figure S12b, Supporting Information) reveals a slope value (b) of 0.88, suggesting that the kinetics of sulfur conversion are dominated by active transport/convective and not diffusive.

To estimate the sulfur utilization and the kinetics of the sulfur conversion reaction quantitatively, the materials were subjected to continuous galvanostatic tests within the potential window of 0.01–2.5 V versus Na/Na^+. In the first cycle, coulombic

efficiency (CE) (Figure S13a, Supporting Information) gradually increases at a larger S/linalool ratio, with the irreversible capacity loss mainly attributed to the electrolyte decomposition on the surface of the carbon.[32,55] The activation process observed in CV is also manifested during the first galvanostatic cycles (Figure 3b). Reaching a low cut-off potential close to 0 V versus Na/Na^+ is key to overcoming the high energy barrier required for sodium transport into the ultra-micropores of pseudo graphitic carbon. After five cycles, the system reaches an equilibrium state, at which the concentration of sodium inside the pores becomes sufficient to react with all confined sulfur species. The high activation energy barrier required for the insertion of Na^+ into the carbon structure and accessing confined sulfur species can be an additional indication of a quasi-solid-state reaction that affects the kinetics.

The galvanostatic curves for S:Lin 50/50 and S:Lin 70/30 materials exhibit a predominantly non-Faradaic capacitive behavior manifested in a sloped shape (Figure 3c), with discharge capacities of 203 and 215 mAh g^{-1} respectively, pointing to the adsorption of sodium on the surface of the carbon.[55–58] In contrast, S:Lin 80/20 and S:Lin 90/10 exhibit two distinct plateau regions between 2.0 and 1.0 V, indicative of the electrochemical reaction between sulfur and sodium and consistent with the CV results. The presence of the plateaus indicates that the conversion of sulfur to Na_2S occurs in two subsequent steps with the formation of intermediate polysulfide species. The capacities of S:Lin 80/20 and S:Lin 90/10 are nearly tripled with respect to S:Lin 50/50 and S:Lin 70/30 materials, providing 510 and 580 mAh g^{-1} at 60 mA g^{-1} current density, respectively, thus pointing to a higher reactivity of sulfur.

Materials with more effective sulfur confinement are expected to offer high rate capability, long-term stability, and a nearly quantitative sulfur utilization. Indeed, S:Lin 80/20 and S:Lin 90/10 maintain unusually high capacities of 346 and 357 mAh g^{-1} at 50 folds larger current densities (3 A g^{-1}), respectively (Figure 3d). Such high rate performance of the SCs is related to the faster kinetics of the quasi-solid state transition between the soluble Na_2S_x (where $x \geq 3$) polysulfides and Na_2S, where the reactivity of the sulfur is increased by means of the confinement achieved in subnanometer sized cavities. This agrees with the small size of the pores (< 0.7 nm) able to accommodate only desolvated Na^+ ions, shifting the reaction to quasi solid state that considerably shortens the electronic transport lengths.[33,51] Furthermore, high electrical conductivity provided by the conjugated carbon matrix formed during thermal condensation ensures effective electron transfer to poorly conductive sulfur species (Table S3, Supporting Information).

To gain a deeper understanding of the difference in the mechanism of electrochemical processes in S:Lin 50/50 and S:Lin 90/10, the materials tested in the cells and charged to 3 V (vs Na/Na^+) were subjected to XPS analysis. The S:Lin 90/10 sample (Figure 3e) exhibits a broad S2p signal deconvoluted to 4 doublets ($2p_{1/2}$-$2p_{3/2}$): Na_2S (159.3 and 160.5 eV), Na_2S_x polysulfides (161.3 and 162.5 eV), C—S/S—S bonds (163.8 and 165 eV) and —C—SO_x groups (168 and 169.2 eV). The dominant contribution from C—S/S—S suggests that the major fraction of the sulfur recovers its initial chemical state in the carbon-sulfur matrix at the fully charged state. In contrast, the S2p spectrum for S:Lin 50/50 reveals the presence of Na_2S_2 polysulfides but no signs of C—S/S—S bonds at 3.0 V. Therefore, the reaction manifested in a single pair of redox peaks in CVs corresponds to the transformation of Na_2S_2 polysulfides to Na_2S, where the first is formed during cleavage of —S—S— and C—S thioether bonds in the initial cycle.

The comparison of C1s XPS spectra for the electrodes charged to 3.0 V additionally supports a significant reduction of C—S bonds for S:Lin 50/50 as compared to S:Lin 90/10 material (Figure S14, Supporting Information). Furthermore, a comparison of the S2p XPS peak for S:Lin 90/10 electrode at different charging states (Figure S15, Supporting Information) shows a disappearance of the C—S/S—S signal at ≈163.8 eV during sodiation and its gradual recovery during desodiation. This reinforces the full transformation of covalent C—S bonds to polysulfides and Na_2S upon discharge and their reversible formation during the charging process.

The results of CV and galvanostatic tests suggest that the charge storage mechanism in S:Lin arises from three major contributions: 1) the dominant faradaic processes of the long-chain sulfur conversion at high voltage (0.8–3.0 V, vs Na/Na^+),[51,59] 2) the reaction of Na^+ with the conjugated carbon backbone and the adsorption of Na^+ ions at defects and within interlayers of microporous hard carbon (0.1–1.6 V, vs Na/Na^+) and 3) insertion of Na^+ in the pore structure of the carbon at low voltage range (0.01–0.1 V, vs Na/Na^+).[60,61] A gradual decrease of the cut-off voltage from 0.01 to 0.75 V (vs Na/Na^+) results in a slight reduction in the intensity of the first redox couple located at 1.1/1.9 V (vs Na/Na^+) (Figure S16, Supporting Information). This suggests that the reversible conversion of long-chain sulfur to polysulfides occurs over a wide potential range and partially overlaps with the reaction between Na^+ and the carbon framework. Full conversion of sulfur in the SC can be achieved only below 0.5 V (vs Na/Na^+), which is substantially lower than the typical reaction potential of elemental sulfur (usually above 1.0 V vs Na/Na^+).[51,59] This is attributed to the effect of the confinement where the sulfur is isolated in subnanometer microcavities, which can accommodate only a few sodium ions at a time. This, on one side, translates to the stabilization of intermediate polysulfide products between the carbon walls, while requiring extended potential range for further reaction and complete conversion to Na_2S.

To explore the evolution of the sulfur-carbon structure during battery cycling, *in operando* Raman spectroscopy test was performed during constant current charge-discharge. The major differences are manifested in a considerable red shift of the G band, simultaneously causing a relative weakening of the D band during discharge from 3 to 0 V and particularly pronounced at voltages below 1.1 V (Figure S17, Supporting Information). Adsorption of Na ions on the carbon surface and defect sites leads to localized charge transfer, weakening the C—C bonds and reducing their vibrational frequencies, contributing to the significant shift of the G peak. Many of these ion adsorption sites are expected to arise from the reversible cleavage of the C—S bond during the formation of sodium polysulfides. Leaving sulfur groups causes a redistribution of electronic charge within the carbon matrix and the formation of structural defects on the pseudo graphitic layers, creating preferential sites for Na^+ adsorption. Notably, these changes are reversible (upon desodiation) and persist in subsequent cycles. These findings elucidate the interdependent properties of the carbon matrix and sulfur phase in the conjugated

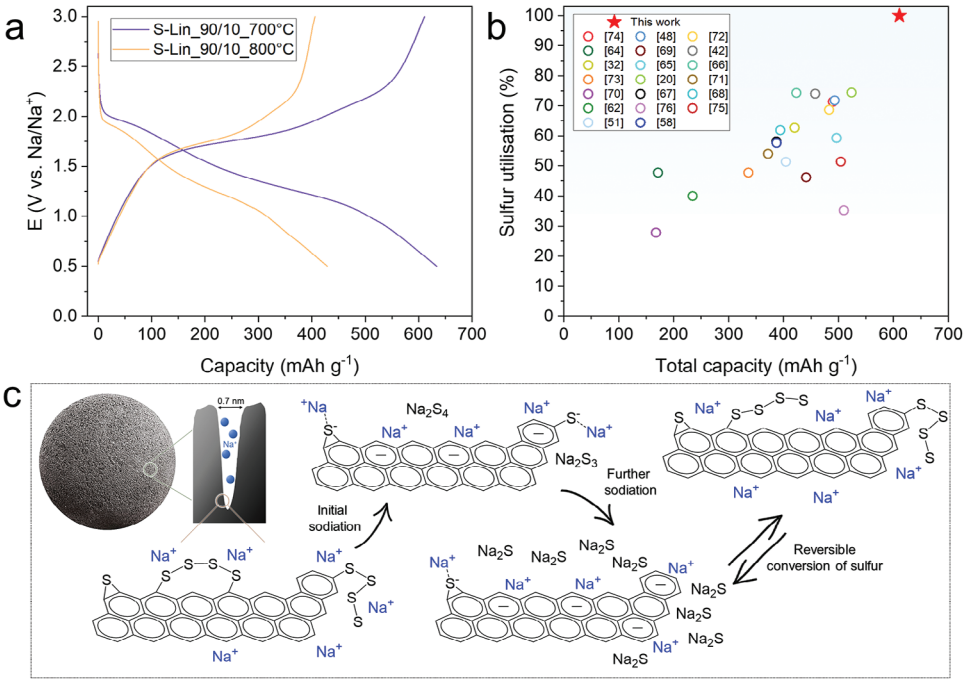

Figure 4. Electrochemical evaluation of sulfur efficiency for Na_2S conversion reaction (capacity values are normalized by the total weight of SC). a) comparison of galvanostatic profiles at 60 mA g^{-1} for S:Lin 90/10 sulfur carbons thermally condensed at 800 and 700 °C, b) comparison of the sulfur utilization versus total capacity for the S:Lin 90/10 700 °C electrode and sulfur–carbon cathodes reported in literature[20,32,42,48,51,58,62,64–76] (the total capacity values from the literature were calculated by multiplying the reported capacity normalized by sulfur weight (mAh g_s^{-1}) by the sulfur loading).

hybrid structure of the S:Lin sulfur carbons during the charging process.

The effect of the chemical structure of the carbon source on the behavior of the final sulfur carbon material was also investigated by using different naturally derived terpenes, varying in the number of vinylic groups, molecular weight, and oxygen-containing functionalities. The resulting materials show diverse morphologies that correlate with the electrochemical behavior in CV and galvanostatic tests (Figures S18–S20, Supporting Information).

The temperature processing of the sulfur carbon and the stability of the confined sulfur at 800 °C are the key factors enabling both the large capacity values and the high rate performance. In contrast to previous studies in which SCs are normally produced at 500–650 °C,[27,43,48,53,55,58,62–64] the higher condensation temperature in this work ensures a higher degree of carbon graphitisation. However, owing to the unique structure of S:Lin, a reduction in the thermal condensation temperature enables a larger sulfur content in the material without compromising the level of sulfur utilization. To demonstrate the effect of thermal treatment on the properties of the SCs, the S:Lin 90/10 copolymer was thermally condensed at 700 °C. At this lower temperature, sulfur loading in the material rose to 32 wt.% (Table S4, Supporting Information), translating to a substantial increase in the capacity observed in GCD (**Figure** 4a) and CV (Figures S21 and S22a, Supporting Information) tests. With the decrease of the thermal condensation temperature, the reversible capacity of the S-Lin 90/10 700 °C cathode reached 611 mAh g^{-1} at 60 mA g^{-1}. By contrast, an elevation of the temperature to 900 °C leads to a further loss of sulfur and a substantial decrease in capacity (Figure S21 and Table S2, Supporting Information).

In order to estimate the efficiency of sulfur utilization, the capacity of the cathode material is typically normalized by the weight of sulfur, assuming that the contribution of the carbon host > 0.5 V is negligible. However, this approach can be misleading for materials with comparable loadings of sulfur and carbon and even more for covalently bonded SC composite materials, where sulfur is incorporated into a conjugated carbon skeleton. Therefore, the total capacity should be represented as a sum of the charge from the sulfur redox process (Q_s) and sodiation/desodiation of hard carbon (Q_c): $Q_{tot} = Q_s{}^* m_s + Q_c{}^* m_c$, where m_s and m_c are mass fractions of sulfur and carbon in the composite material, respectively. For comparison, we subtracted the maximum capacity of a disordered hard carbon in Na-ion batteries above 0.5 V (vs Na/Na^+) is ≈120 mAh g^{-1}, which is rarely achieved even during the first irreversible discharge.[77,78] This leads to a capacity value of 1655 mAh $g_{(s)}^{-1}$, which approaches the theoretical value corresponding to 99% sulfur utilization (see Supporting Information for the detailed calculations). Even at higher cut-off potentials of 0.75 and 1.0 V (vs Na/Na^+), the material still exhibits high reversible capacity values of 524 and 452 mAh g^{-1}, respectively (Figure S22b, Supporting Information). In the full potential range from 0.01 to 3.0 V, the electrode achieves a discharge capacity of 820 mAh g^{-1} by taking advantage of the capacitive contribution of the conjugated carbon framework. High capacity values are maintained even at large mass loadings of the active material (3–12 mg cm^{-2}), making S:Lin sulfur carbon a promising cathode material for practical applications (Figure S23, Supporting Information).

The storage capacity remains high at very fast charging rates: 85% at 600 mA g^{-1} and 66% at 6 A g^{-1} (Figures S22c,d,

Supporting Information), reflecting the fast kinetics of the material preserved even at the reduced temperature of thermal condensation. The rapid electron transport in the sulfur carbon is promoted by the conductive turbostratic graphitic-like structure of carbon that remains preserved at 700 °C (Figure S24, Supporting Information). Remarkably, a reversible capacity of 370 mAh g^{-1} was still achieved at 15 A g^{-1}, showing the high reactivity of the sulfur confined in the ultramicro pores.

When compared to the literature, S:Lin 90/10 700 °C material considerably outperforms all the reported cathode materials for room temperature Na-S batteries (Figure 4b). The capacity values normalized by the sulfur weight are usually below 1000–1200 mAh $g_{(s)}^{-1}$, as compared to ≈1655 mAh $g_{(s)}^{-1}$ for the sulfur carbon derived from the sulfur-linalool copolymer presented here, corresponding to ≈100% sulfur utilisation (Figure S25a, Supporting Information). Normalizing by the total weight of the cathode material, the S:Lin 90/10 700 °C electrode delivers the highest reported capacity among RT Na-S battery cathodes at considerably lower sulfur loading (Figure S25b, Supporting Information). When tested in the full potential range (0.01–3.0 V), the material also exhibits the largest performance when compared to state-of-the-art carbon-sulfur cathodes (Table S4, Supporting Information). This indicates that the unique structure of the sulfur carbon composite, with highly active sulfur and thioether groups bonded to graphitic-like layers of the hard carbon, maximizes the efficiency and reversibility of $S^0 \rightarrow Na_2S_x \rightarrow Na_2S$ conversion reactions.

The schematic in Figure 4c illustrates the chemical transformations occurring within the material during the charging process. Sulfur chains, confined within the nanocavities of the conductive carbon matrix and covalently anchored to the carbon layers, are cleaved upon sodiation. This cleavage is accompanied by the formation of sodium polysulfide species, which are stepwise converted to Na_2S_2 and subsequently to Na_2S at lower potentials. At the same time, the cleavage of C—S bonds causes a redistribution of electronic charge within the carbon matrix. This process results in the formation of structural defects at the edges of pseudo graphitic layers, creating preferential sites for Na^+ adsorption, which is combined with the adsorption of Na^+ ions on the surface of the layers. The reaction is fully reversible, with sulfur—carbon bonds reforming during the desodiation process. Therefore, the high electrochemical performance of the material is achieved through structural optimization of SC architecture where most of the sulfur atoms participate in faradaic energy storage.

To better understand the interactions between sulfur species and Na ions within the hybrid material, we employed AIMD simulations and DFT calculations. For that, the geometry and energy characteristics were evaluated during Na insertion into a periodic graphene bilayer with dangling sulfur chains (Figure S26, Supporting Information), analogous to the pure carbon configurations examined in our previous work.[79,80] Na atoms were inserted into the structure at various concentrations and optimized. In all systems and throughout all AIMD simulations the sulfur atoms directly bonded to the edges of the graphene (C—S and C—S—S—C) are extremely stable, remaining attached to the edges and not participating in the formation of Na-S species. In contrast, the long-chain sulfur atoms can detach within extremely short timescales (≈3 ps) and participate in reactions with the incoming Na.

Figure 5a,b depict the formation enthalpies of the sodiated system and corresponding voltage profile versus Na/Na^+. Following the lowest enthalpy path, a first-order phase transition between the empty sulfated bilayer ($S_{50}C_{127}$) and $Na_9S_{50}C_{127}$ is observed. During this phase transition, the long chain sulfur becomes coordinated by Na atoms, forming Na-S distances between 2.7 and 2.9 Å (Figure 5c). The Na atom is unrelated to the formation of the NaS clusters and is stabilized between the sulfated edges of opposing graphitic layers at a distance of 2.6–2.7 Å (dotted square in Figure 5c). The $Na_9S_{50}C_{127}$ phase demonstrates the formation of Na-S by the long-chain sulfur atoms, having a total Na/chain-available S ratio of 1.13/1. This phase occurs at a calculated voltage of 1.68 V versus Na metal.

The sodiation mechanism continues with another first-order phase transition, forming the $Na_{24}S_{50}C_{127}$ phase, corresponding to a voltage plateau at 0.99 V. In the optimized configuration (Figure 5d), we observe further dissociation of the chain-available S atoms and denser coordination by Na. In total, 18 Na atoms are associated with this Na-S cluster, with distances ranging from 2.56 to 2.84 Å, corresponding to $Na_{2.13}S$. The remaining 6 Na atoms remain stabilized between the graphitic edges at a distance of 2.6–2.7 Å. Placing more Na in the system continues this type of sodiation of the edges, raising the energy of the system and leading to lower potentials versus Na-metal.

The SC material, produced at a temperature of 700 °C, exhibits remarkable endurance during a cycling test. It maintains its full capacity after 600 cycles at 1 A g^{-1} and 87% (514 mAh g^{-1}) of its initial performance after 1000 cycles (**Figure** 6a). Even after 1500 cycles, the cell retains 440 mAh g^{-1} (80%), demonstrating outstanding long-term stability. Similarly, SC formed at 800 °C exhibits excellent stability achieving only 0.017% capacity decay per cycle (Figure S27a, Supporting Information). The decrease in performance is often caused by several factors, including the degradation of sodium metal, binder, or solvent molecules.[59,81] For instance, the cyclability of cathode the can be considerably increased by replacing the conventional PVDF binder with carboxyl-containing polyacrylic acid (PAA) (Figure S27b, Supporting Information).

The high stability of the cathode material indicates minimal expansion and mechanical stress during sulfur conversion, another key advantage of nanoconfined sulfur. After 1500 galvanostatic cycles, SEM analysis of the S:Lin 90/10 700 °C surface shows a morphology similar to the original sulfur carbon, with the material's structural integrity remaining intact despite repeated sodiation–desodiation. (Figure 6a; Figure S28, Supporting Information). HRTEM images (Figure S29, Supporting Information) confirm the nanostructure's integrity, revealing a similar turbostratic structure with no structural degradation. TEM fringe analysis estimates the interlayer distance for both samples to be 0.35–0.40 nm, indicating no interlayer swelling after the long cycling test. In operando WAXS analysis supports this, showing no significant shift, nor fading of the (002) peak during charge and discharge (Figure S30, Supporting Information).

Elemental sulfur has a density of ≈2 g cm^{-3}, depending on the allotropes. In small micropores, dense allotropes cannot form and pack, while even some very small micropores will not fill with sulfur at all, so we may expect more disordered and lower-density

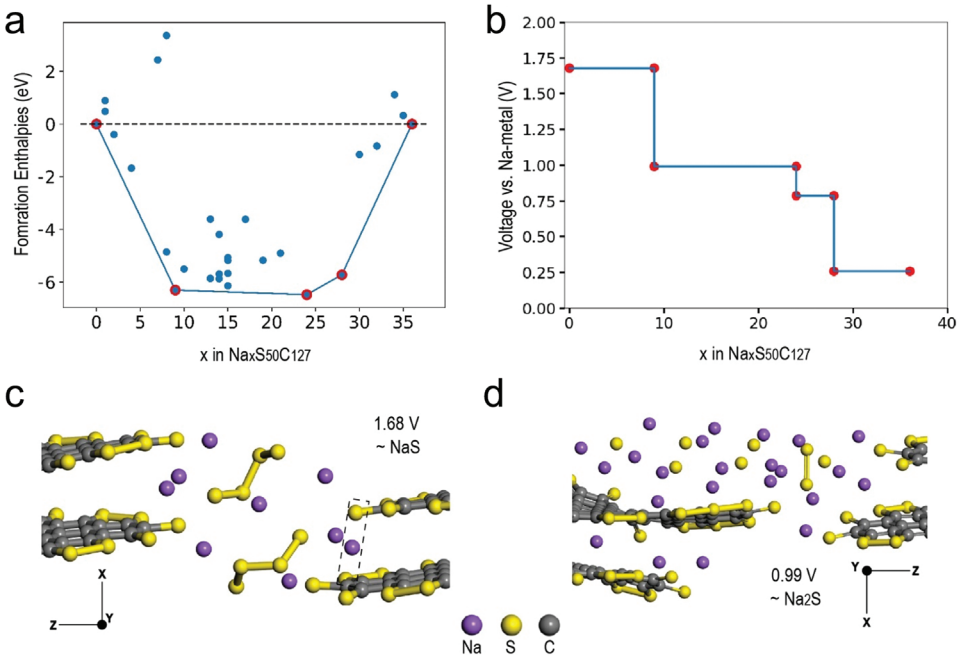

Figure 5. DFT calculations of Na interactions with long sulfur chains at the edges of graphitic layers. a) formation enthalpies of the $Na_xS_{50}C_{127}$ structure, b) voltage profile of the $Na_xS_{50}C_{127}$ structure versus Na/Na^+, c) $Na_9S_{50}C_{127}$ optimized configuration at 1.68 V, the dotted square indicates the Na that is not related to the Na-S cluster and d) $Na_{24}S_{50}C_{127}$ optimized configuration at 0.99 V.

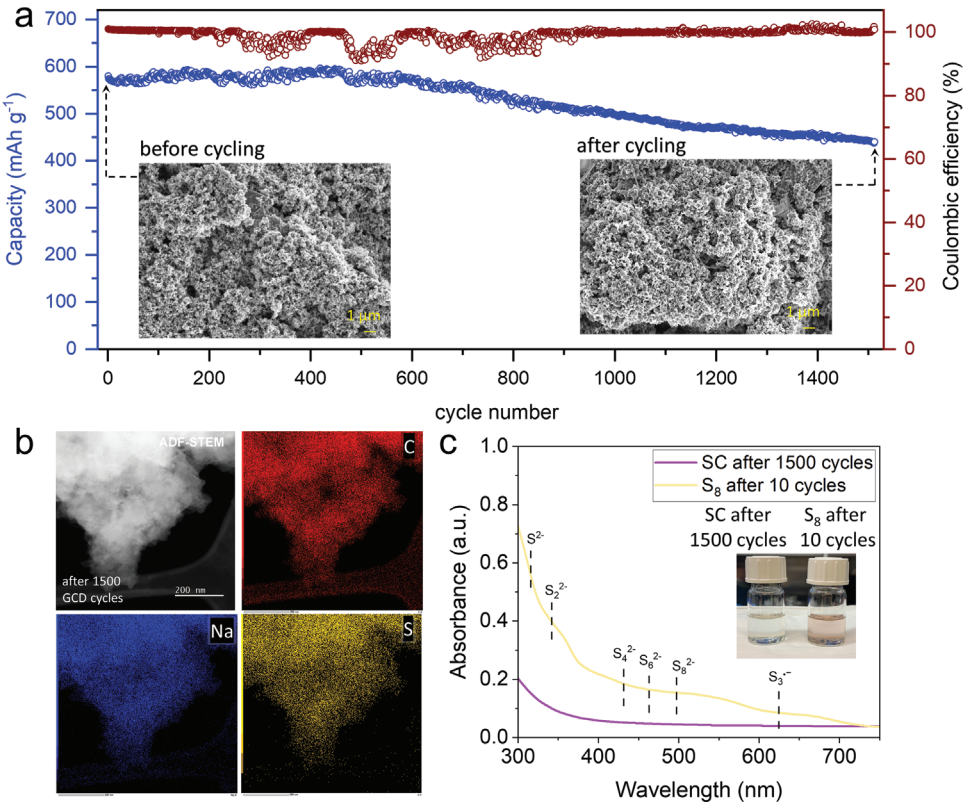

Figure 6. Long-term stability test. a) cycling performance of S:Lin 90/10 700 °C cathode material at 1 A g^{-1} (inset: SEM images comparing morphology of S:Lin 90/10 700 °C electrode before and after 1500 galvanostatic cycles), b) TEM-EDS mapping showing elemental composition of the SC electrode after cycling and c) UV/Vis absorption spectra and images of two solutions prepared after washing the components of the Na-S cells with SC (S-Lin 90/100 700 °C) cathode after 1500 galvanostatic cycles and elemental sulfur cathode after 10 galvanostatic cycles.

structures. The density of Na_2S is 1.86 g cm^{-3}, and it remains a question to answer how Na_2S is located in the nanopore system.

The stability of sulfur species within the sample was examined using EDS analysis at both the nanoscale (TEM-EDS) and microscale (SEM-EDS). Elemental mapping demonstrates that sulfur remains uniformly distributed within the carbon matrix (Figure 6b; Figures S31–S36, Supporting Information). Statistical EDS analysis of electrodes, both after initial activation (10 GCD cycles) and after extensive cycling (1500 GCD cycles), shows only a minor reduction in the sulfur-to-carbon ratio (Table S6, Supporting Information). In contrast, cathode material prepared with elemental sulfur exhibits a significant loss of sulfur after just 10 galvanostatic cycles (Figure S37, Supporting Information). These findings confirm that a substantial portion of sulfur remains intact throughout extensive cycling, indicating effective chemical and physical confinement of the sulfur species.

The presence of dissolved polysulfides in the electrolyte after a few galvanostatic cycles of the elemental sulfur electrode was also confirmed by UV–vis absorption spectroscopy (Figure 6c). In contrast, a colorless transparent solution obtained by thoroughly washing all cell components, including S:Lin 90/10 700 °C cathode subjected to 1500 galvanostatic cycles, has a weak UV–vis absorbance, confirming negligible dissolution and shuttling of polysulfides and active material into the electrolyte. In addition, a visual GCD cycling test of the S:Lin 90/10 700 °C cathode in a quartz cuvette shows no change in the color of the electrolyte solution after continuous cycling over 17 days, confirming the high stability of the confined sulfur species (Figure S38, Supporting Information). These results further reinforce the evidence of an efficient immobilization of sulfur via physical confinement, leading to an excellent electrochemical performance of the SC as a cathode in RT-Na/S batteries.

3. Conclusions

In this work, a new facile, inexpensive, and sustainable approach to producing a sulfur-carbon (SC) material with nanoconfined sulfur species via one-pot inverse vulcanization-condensation of a sulfur-linalool mixture is introduced. The unique structure of the SC, with highly active sulfur chains constrained within nanocavities of a conductive carbon matrix, maximizes the efficiency and the kinetics of the $S \rightarrow Na_2S_x \rightarrow Na_2S$ reactions while stabilizing the intermediate products. The resulting material delivers 611 mAh g^{-1} from the electrochemical conversion of sulfur and sodium, corresponding to the highest reported reversible capacity up to now. The high reactivity of effectively confined sulfur molecules manifests in ≈100% sulfur utilization, with a normalized sulfur capacity of 1655 mAh $g_{(s)}^{-1}$ approaching the theoretical limit. The fast kinetics and exceptional stability of quasi-solid-state reaction in confined space translates to an outstanding rate capability of the SC and one of the longest cycling stabilities with 87% capacity retention over 1000 cycles at 1 A g^{-1}.

These results demonstrate an innovative approach to fabricating sulfur–carbon structures with highly active S sites confined in a conductive carbon matrix using naturally abundant materials. We envision that this method has the potential for scale-up and could be further applied to a range of similar plant-derived terpenes with vinylic groups. Overall, this strategy opens up a new avenue to a high-performance electrochemical energy storage material with high-energy and long cycle life. On the other hand, it also indicates the potential of reactions in confined spaces to simplify and direct reaction pathways.

4. Experimental Section

Inverse Vulcanization/Thermal Condensation of Sulfur and Linalool: Sulfur and linalool were mixed in cylindrical ceramic crucibles (50 mm diameter, 34 ml volume) at different weight ratios and were transferred to a furnace. The muffle furnace was flushed with nitrogen gas for 1 h before heating. The samples were heated in a nitrogen atmosphere with a gas flow of 2 L min^{-1} at the rate of 180 °C h^{-1} first to 175 °C with 20 min dwelling time and then directly subjected to 800 °C held for 2 h. The sulfur copolymers were formed at 175 °C via inverse vulcanization and further thermally condensed at 800 °C in a single step. The resultant sulfur carbon material was ground to a fine powder and further used as active cathode material.

Materials Characterization: The morphology of the samples was analyzed by scanning electron microscope (Zeiss LEO 1550-Gemini) at an acceleration voltage of 3 kV. Energy-dispersive X-ray measurements were collected with Oxford Instruments X-MAX 80 mm^2 detector. High-resolution transmission electron microscopy (HRTEM) images and electron energy loss spectra (EELS) were acquired with a double aberration-corrected Jeol JEM ARM200F microscope, equipped with a cold field emission gun, and a GIF Quantum from Gatan, operated at 80 kV. The data was analyzed by Gatan's microscopy suite (GMS) software, version 3.4. Raman spectra of the samples were measured using a WITec Alpha 300 Raman spectrometer equipped with a 532 nm (2.33 eV) excitation laser source. XPS data were obtained from a K-alpha$^+$ XPS spectrometer (Thermo Fisher Scientific) with a monochromatic Al Kα ($h\nu$ = 1486.6 eV) X-ray source. To fit the XPS spectra, Shirley background profile subtraction was applied and peaks were fitted using Gaussian/Lorentzian shapes. All XPS spectra were corrected by referencing the fitted contribution of C—C graphitic carbon in the C1s signal 284.5 eV. Thermogravimetric analysis was performed under N_2 gas in NETZSCH TG-209 Libra at a heating rate of 10 °C min^{-1}. Physisorption of the samples was measured with Quantachrome Instrument (Quadrasorb SI) at 77 K for N_2 and 273 K for CO_2. The samples were previously degassed at 150 °C under vacuum for 20 h. The data was analyzed using Quadrachrome QuadraWin software, version 5.11. For N_2 sorption results, the specific surface area was calculated by applying the Brunauer–Emmett–Teller (BET) model to the isotherm data points of the adsorption branch in the relative pressure range $p/p_0 < 0.3$. Micropore volume (V_{micro}) was calculated by the t-pot method and total pore volume (V_{tot}) was obtained from isotherm data at the highest relative pressure achieved. Pore size distribution was determined by applying the Quantized Liquid Density-Functional Theory (QLDFT) model to the adsorption branch of the isotherm. For CO_2 sorption, specific surface area and pore size distribution were estimated using the Non-Local Density-Functional Theory (NLDFT) model. Elemental analysis measurements were performed using Elementar Vario EL III instrument with combustive mode for quantifying the amount of carbon, hydrogen, nitrogen, and sulfur; and non-combustive for quantifying the content of oxygen in the samples. The XRD patterns were collected with Rigaku SmartLab equipped with Cu Kα radiation (λ = 1.54 Å). Proton nuclear magnetic resonance (1H-NMR) spectra were recorded at ambient temperature using a Bruker Ascend 400 MHz NMR spectrometer. The molecular weight of the sulfur copolymers was determined by gel permeation chromatography (GPC) with THF as an eluent and polystyrene standard. UV–vis absorption spectra were acquired using Shimadzu UV 2600 in diffuse reflectance mode. The solutions of the cycled cells subjected to UV–vis analysis were obtained by thoroughly washing all components of the cells with the propylene carbonate solvent in the glovebox over a week. The final solutions from two cells (S-Lin 90/10 and elemental sulfur) were further diluted to achieve the same concentration of sulfur. The postcycling analyses of the cathodes were performed after washing with the carbonate-based solvent over a week and drying in the argon-filled glovebox.

Electrochemical Measurements: The working electrodes were produced by mixing thermally condensed sulfur-carbons, conductive carbon black, and polyvinylidene difluoride (PVDF) in N-methyl-2-pyrrolidine (NMP) at a weight ratio of 7:2:1. The obtained slurry was cast onto an aluminum foil (15 µm) using an automatic doctor blade film applicator and dried overnight at 60 °C in a vacuum oven. The normal electrode material mass loading was 0.8–1.2 mg cm^{-2}. High mass loading electrodes (3 mg cm^{-2}) were prepared with the same method and the slurry composition. To achieve 12.2 mg cm^{-2} mass loading of active material, Ni mesh (95% porosity, 80–110 pores per inch. average hole diameters ≈0.25 mm) was dip-coated into the same slurry and further dried. The same experimental procedure was used to prepare an electrode with a PAA-based aqueous binder, which was employed only once for S-Lin 90/10 800 °C cathode material. All electrochemical testing was performed using Swagelok cells on a Biologic MPG-2 instrument at room temperature. The cells were assembled in an argon-filled glovebox with H_2O and O_2 content <0.1 ppm. S:Lin electrodes were punched to circular electrodes (diameter of 0.6 cm) and employed as working electrodes. The cells were assembled by sandwiching a glass fiber (Whatman GF/C) separator between the working electrode and a thin disc of sodium metal (99.5%, Sigma–Aldrich) used as a counter and reference electrode impregnated with 200 µl of electrolyte. The electrolyte was composed of 1 M $NaClO_4$ in ethylene carbonate (EC) and propylene carbonate (PC) (50:50 in vol.%) with 5 wt.% of fluoroethylene carbonate (FEC).

Cyclic voltammogram (CV) measurements were performed over a potential range from 0.01 to 3 V and scan rates of 0.1–2 mV s^{-1}. Electrochemical impedance spectra (EIS) were obtained in the frequency range from 100 kHz to 100 MHz at a potential amplitude of 10 mV and varied bias voltage. Galvanostatic tests were performed at different current densities from 60 to 15,000 mA g^{-1} and at different cutoff voltage within 0.01–3.0 V window (vs Na^+/Na).

In Operando Wide-Angle X-Ray Scattering (WAXS): In operando WAXS measurements were performed using a Bruker Nanostar II instrument (USA) with Cu Kα radiation (wavelength 0.154 nm), 50 kV voltage, and 600 µA current. The sample-to-detector distance was calibrated using a glassy carbon reference (NIST SRM3600) and was roughly 54 mm, providing a q-range of $\approx 3.5 < q < 40$ nm^{-1}. The focal spot size of the beam was 115 µm. The measurements were performed using a specialized cell in transmission mode with Kapton film as windows. WAXS patterns were collected every 30 min providing a total number of counts $\approx 0.9\text{-}1.1 \times 10^6$ counts. Data reduction involved azimuthal integration to extract 1D scattering profiles and subtract the background (cell without active material). Scattering data were corrected for transmission and primary beam intensity and scaled to absolute intensity units.

In Operando Raman Spectroscopy: In operando Raman spectroscopy was performed using the WITec Alpha 300R (Germany) confocal Raman microscope with a laser wavelength of 532 nm and a compression-controlled Raman battery cell (Redoxme AB, Sweden) with a sapphire window. To avoid the possible contribution of conductive carbon additive, the electrodes were prepared using only active material and binder. Spectra were collected every 10 s with a reduced laser power of 1 mW to avoid degradation of the sample and electrolyte.

Density Functional Theory (DFT) Calculations: Density functional theory (DFT) calculations based on the Perdew–Burke–Ernzerhof (PBE) functional[82] within the Vienna Ab initio Simulation Package (VASP)[83] Projector augmented wave (PAW) potentials[84] were employed with [Ne] cores for Na and S and [He] for C. All calculations were initialized as spin-polarised. DFT relaxations were performed with a cutoff energy of 400 eV, a 2 × 2 × 1 k-point mesh, and dispersion force contributions formulated by Grimme.[85] Ab initio molecular dynamics (AIMD) simulations were performed in the canonical (NVT) ensemble using the Nosé-Hoover thermostat[86,87] using a cutoff energy of 300 eV and a gamma-only k-point mesh.

A periodic graphene superstructure with sulfur dangling chains was constructed analogously to the pure carbon configurations examined in the previous work.[79,80] This structure included two graphene sheets with edges terminated by sulfur atoms, along with 8 excess sulfur atoms that do not have available dangling carbon bonds to attach to, thus forming chains. The superstructure was initially optimized using AIMD simulations for 8 ps at 400 K, stabilizing in the configuration depicted in Figure S26a (Supporting Information). It contained 177 atoms (50 S and 127 C), with dimensions of 2.24 × 2.47 × 3.00 nm and a gamma angle of 120° (Figure S26b, Supporting Information).

To predict how Na atoms would dissipate and interact with the sulfated graphene sheets, AIMD simulations were conducted with Na atoms inserted at various concentrations (4, 8, 16, 24, 36 atoms). The simulations were performed at 400 K for 8 ps to allow optimal diffusion and reaction of Na with the host structure. Stabilization of all systems, indicating where Na resides and reacts, was observed early, ≈3–4 ps into the simulation. Subsequently, the MD-optimized configurations were further relaxed using DFT calculations to obtain total energies. Similar configurations were also tested, varying in Na content, based on the MD-optimized ones. The calculated energies were used to construct the convex hull diagram,[88] indicating the enthalpies of formation of the Na—sulfated carbon system, and to calculate the corresponding voltage[89] versus Na metal.

Supporting Information

Supporting Information is available from the Wiley Online Library or from the author.

Acknowledgements

This research has received funding from the European Research Council (ERC) under the European Union's Horizon 2020 research and innovation program, MoMa-STOR (Grant agreement No: 951513). The authors thank the Max Planck Society for funding. Financial support within the Max Planck-Fraunhofer Cooperation program (CLUSTERBATT) is gratefully acknowledged. The authors would like to express their gratitude to the Lorentz Center Workshop "Electrochemical Energy Storage in 2D and Layered Materials". Special thanks to Irina Shekova for the physisorption measurements, Bolortuya Badamdorj for scanning electron microscopy imagining, and Antje Völkel for the elemental analysis and thermogravimetric analysis.

Open access funding enabled and organized by Projekt DEAL.

Conflict of Interest

The authors declare no conflict of interest.

Data Availability Statement

The data that support the findings of this study are available from the corresponding author upon reasonable request.

Keywords

electrochemical energy storage, inverse vulcanisation, nanoconfinement, sodium-sulfur reaction, sulfur, sustainable

Received: August 27, 2024
Revised: October 1, 2024
Published online:

[1] A. B. Grommet, M. Feller, R. Klajn, *Nat. Nanotechnol.* **2020**, *15*, 256.
[2] K. A. Henzler-Wildman, V. Thai, M. Lei, M. Ott, M. Wolf-Watz, T. Fenn, E. Pozharski, M. A. Wilson, G. A. Petsko, M. Karplus, *Nature* **2007**, *450*, 838.

[3] Y. Huang, J. Ren, X. Qu, *Chem. Rev.* **2019**, *119*, 4357.
[4] V. Kapil, C. Schran, A. Zen, J. Chen, C. J. Pickard, A. Michaelides, *Nature* **2022**, *609*, 512.
[5] H. Li, J. Xiao, Q. Fu, X. Bao, *Proc. Natl. Acad. Sci.* **2017**, *114*, 5930.
[6] Q. Zhang, S. Gao, J. Yu, *Chem. Rev.* **2022**, *123*, 6039.
[7] B. Smit, T. L. M. Maesen, *Nature* **2008**, *451*, 671.
[8] M. Dusselier, P. Van Wouwe, A. Dewaele, P. A. Jacobs, B. F. Sels, *Science* **2015**, *349*, 78.
[9] Z. Jin, L. Wang, E. Zuidema, K. Mondal, M. Zhang, J. Zhang, C. Wang, X. Meng, H. Yang, C. Mesters, *Science* **2020**, *367*, 193.
[10] Q.-Q. Wang, S. Gonell, S. H. A. M. Leenders, M. Dürr, I. Ivanović-Burmazović, J. N. H. Reek, *Nat. Chem.* **2016**, *8*, 225.
[11] B. Chatelet, H. Gornitzka, V. Dufaud, E. Jeanneau, J.-P. Dutasta, A. Martinez, *J. Am. Chem. Soc.* **2013**, *135*, 18659.
[12] L.-J. Chen, S. Chen, Y. Qin, L. Xu, G.-Q. Yin, J.-L. Zhu, F.-F. Zhu, W. Zheng, X. Li, H.-B. Yang, *J. Am. Chem. Soc.* **2018**, *140*, 5049.
[13] W. Liu, D. Lin, A. Pei, Y. Cui, *J. Am. Chem. Soc.* **2016**, *138*, 15443.
[14] T. Tang, Y. Hou, *Small Methods* **2020**, *4*, 1900001.
[15] L. Liu, U. Diaz, R. Arenal, G. Agostini, P. Concepcion, A. Corma, *Nat. Mater.* **2017**, *16*, 132.
[16] Z. Huang, W. Wang, W. Song, M. Wang, H. Chen, S. Jiao, D. Fang, *Angew. Chemie* **2022**, *134*, 202202696.
[17] S. Xin, L. Gu, N.-H. Zhao, Y.-X. Yin, L.-J. Zhou, Y.-G. Guo, L.-J. Wan, *J. Am. Chem. Soc.* **2012**, *134*, 18510.
[18] C. Y. J. Lim, Z. W. Seh, *Battery Energy* **2022**, *1*, 20220008.
[19] F. Xiao, X. Yang, H. Wang, J. Xu, Y. Liu, D. Y. W. Yu, A. L. Rogach, *Adv. Energy Mater.* **2020**, *10*, 2000931.
[20] Q. Guo, S. Li, X. Liu, H. Lu, X. Chang, H. Zhang, X. Zhu, Q. Xia, C. Yan, H. Xia, *Adv. Sci.* **2020**, *7*, 1903246.
[21] L. Zhou, D. L. Danilov, R. Eichel, P. H. L. Notten, *Adv. Energy Mater.* **2021**, *11*, 2001304.
[22] R. Rathnayake, T. T. Duignan, D. J. Searles, X. S. Zhao, *Phys. Chem. Chem. Phys.* **2021**, *23*, 3063.
[23] E. Oğuzhan Eren, C. Esen, E. Scoppola, Z. Song, E. Senokos, H. Zschiesche, D. Cruz, I. Lauermann, N. V. Tarakina, B. Kumru, M. Antonietti, P. Giusto, *Adv. Sci.* **2024**, *11*, 2310196.
[24] C. Li, Y. Sun, Q. Wu, X. Liang, C. Chen, H. Xiang, *Chem. Commun.* **2020**, *56*, 6078.
[25] X. Dou, I. Hasa, D. Saurel, C. Vaalma, L. Wu, D. Buchholz, D. Bresser, S. Komaba, S. Passerini, *Mater. Today* **2019**, *23*, 87.
[26] X. Lin, Y. Liu, H. Tan, B. Zhang, *Carbon* **2020**, *157*, 316.
[27] W. Li, M. Zhou, H. Li, K. Wang, S. Cheng, K. Jiang, *Energy Environ. Sci.* **2015**, *8*, 2916.
[28] P. Piaggio, C. Cuniberti, G. Dellepiane, E. Campani, G. Gorini, G. Masetti, M. Novi, G. Petrillo, *Spectrochim. Acta Part A Mol. Spectrosc.* **1989**, *45*, 347.
[29] X. Yu, J. Xie, J. Yang, H. Huang, K. Wang, Z. Wen, *J. Electroanal. Chem.* **2004**, *573*, 121.
[30] Y. Xu, Y. Wen, Y. Zhu, K. Gaskell, K. A. Cychosz, B. Eichhorn, K. Xu, C. Wang, *Adv. Funct. Mater.* **2015**, *25*, 4312.
[31] D.-W. Wang, K.-H. Wu, Y. Li, F. C. de Godoi, I. R. Gentle, *J. Mater. Chem. A* **2014**, *2*, 6439.
[32] S. Xin, Y. Yin, Y. Guo, L. Wan, *Adv. Mater.* **2014**, *26*, 1261.
[33] M. Helen, T. Diemant, S. Schindler, R. J. Behm, M. Danzer, U. Kaiser, M. Fichtner, M. Anji Reddy, *ACS Omega* **2018**, *3*, 11290.
[34] G. Li, J. Sun, W. Hou, S. Jiang, Y. Huang, J. Geng, *Nat. Commun.* **2016**, *7*, 10601.
[35] Z. Wang, Y. Dong, H. Li, Z. Zhao, H. Bin Wu, C. Hao, S. Liu, J. Qiu, X. W. D. Lou, *Nat. Commun.* **2014**, *5*, https://doi.org/10.1038/ncomms6002.
[36] D. Flahaut, M. Minvielle, A. Sambou, P. Lecour, C. Legens, J. Barbier, *Fuel* **2017**, *202*, 307.
[37] M. S. Karunarathna, M. K. Lauer, T. Thiounn, R. C. Smith, A. G. Tennyson, *J. Mater. Chem. A* **2019**, *7*, 15683.
[38] L. Lin, C. Zhang, Y. Huang, Y. Zhuang, M. Fan, J. Lin, L. Wang, Q. Xie, D. Peng, *Small* **2022**, *18*, 2107368.
[39] L. Wang, T. Wang, L. Peng, Y. Wang, M. Zhang, J. Zhou, M. Chen, J. Cao, H. Fei, X. Duan, *Natl. Sci. Rev.* **2022**, *9*, nwab050.
[40] J. Ding, H. Wang, Z. Li, A. Kohandehghan, K. Cui, Z. Xu, B. Zahiri, X. Tan, E. M. Lotfabad, B. C. Olsen, *ACS Nano* **2013**, *7*, 11004.
[41] Y. Cao, L. Xiao, M. L. Sushko, W. Wang, B. Schwenzer, J. Xiao, Z. Nie, L. V. Saraf, Z. Yang, J. Liu, *Nano Lett.* **2012**, *12*, 3783.
[42] J. Yan, W. Li, R. Wang, P. Feng, M. Jiang, J. Han, S. Cao, Z. Zhang, K. Wang, K. Jiang, *ACS Energy Lett.* **2020**, *5*, 1307.
[43] K. Chen, H. Li, Y. Xu, K. Liu, H. Li, X. Xu, X. Qiu, M. Liu, *Nanoscale* **2019**, *11*, 5967.
[44] Z. Yan, L. Zhao, Y. Wang, Z. Zhu, S. Chou, *Adv. Funct. Mater.* **2022**, *32*, 2205622.
[45] N. Wang, Y. Wang, Z. Bai, Z. Fang, X. Zhang, Z. Xu, Y. Ding, X. Xu, Y. Du, S. Dou, *Energy Environ. Sci.* **2020**, *13*, 562.
[46] Y.-X. Wang, J. Yang, W. Lai, S.-L. Chou, Q.-F. Gu, H. K. Liu, D. Zhao, S. X. Dou, *J. Am. Chem. Soc.* **2016**, *138*, 16576.
[47] X. Hu, Y. Ni, C. Wang, H. Wang, E. Matios, J. Chen, W. Li, *Cell Rep. Phys. Sci.* **2020**, *1*, 100015.
[48] S. Li, Z. Zeng, J. Yang, Z. Han, W. Hu, L. Wang, J. Ma, B. Shan, J. Xie, *ACS Appl. Energy Mater.* **2019**, *2*, 2956.
[49] T. Yang, W. Gao, B. Guo, R. Zhan, Q. Xu, H. He, S.-J. Bao, X. Li, Y. Chen, M. Xu, *J. Mater. Chem. A* **2019**, *7*, 150.
[50] J. Zhou, Y. Yang, Y. Zhang, S. Duan, X. Zhou, W. Sun, S. Xu, *Angew. Chem., Int. Ed.* **2021**, *60*, 10129.
[51] S. Wei, S. Xu, A. Agrawral, S. Choudhury, Y. Lu, Z. Tu, L. Ma, L. A. Archer, *Nat. Commun.* **2016**, *7*, 12626.
[52] Z. Li, C. Wang, F. Ling, L. Wang, R. Bai, Y. Shao, Q. Chen, H. Yuan, Y. Yu, Y. Tan, *Adv. Mater.* **2022**, *34*, 2204214.
[53] Y. Lu, J. Liang, Y. Hu, Y. Liu, K. Chen, S. Deng, D. Wang, *Adv. Energy Mater.* **2020**, *10*, 1903312.
[54] A. Kumar, A. Ghosh, A. Ghosh, A. Ahuja, A. Sengupta, M. Forsyth, D. R. MacFarlane, S. Mitra, *Energy Storage Mater.* **2021**, *42*, 608.
[55] J. Yang, X. Zhou, D. Wu, X. Zhao, Z. Zhou, *Adv. Mater.* **2017**, *29*, 1604108.
[56] R. Mishra, S. Panigrahy, S. Barman, *Energy Fuels* **2022**, *36*, 12310.
[57] D. Xu, C. Chen, J. Xie, B. Zhang, L. Miao, J. Cai, Y. Huang, L. Zhang, *Adv. Energy Mater.* **2016**, *6*, 1501929.
[58] T. Wu, M. Jing, L. Yang, G. Zou, H. Hou, Y. Zhang, Y. Zhang, X. Cao, X. Ji, *Adv. Energy Mater.* **2019**, *9*, 1803478.
[59] Y. Wang, B. Zhang, W. Lai, Y. Xu, S. Chou, H. Liu, S. Dou, *Adv. Energy Mater.* **2017**, *7*, 1602829.
[60] C. M. Ghimbeu, J. Górka, V. Simone, L. Simonin, S. Martinet, C. Vix-Guterl, *Nano Energy* **2018**, *44*, 327.
[61] Z. Tian, Y. Zhang, J. Zhu, Q. Li, T. Liu, M. Antonietti, *Adv. Energy Mater.* **2021**, *11*, 2102489.
[62] A. Y. S. Eng, D.-T. Nguyen, V. Kumar, G. S. Subramanian, M.-F. Ng, Z. W. Seh, *J. Mater. Chem. A* **2020**, *8*, 22983.
[63] H. Kim, M. K. Sadan, C. Kim, J. Jo, M. Seong, K.-K. Cho, K.-W. Kim, J.-H. Ahn, H.-J. Ahn, *Chem. Eng. J.* **2021**, *426*, 130787.
[64] T. H. Hwang, D. S. Jung, J.-S. Kim, B. G. Kim, J. W. Choi, *Nano Lett.* **2013**, *13*, 4532.
[65] R. Carter, L. Oakes, A. Douglas, N. Muralidharan, A. P. Cohn, C. L. Pint, *Nano Lett.* **2017**, *17*, 1863.
[66] Y.-M. Chen, W. Liang, S. Li, F. Zou, S. M. Bhaway, Z. Qiang, M. Gao, B. D. Vogt, Y. Zhu, *J. Mater. Chem. A* **2016**, *4*, 12471.
[67] A. Y. S. Eng, Y. Wang, D.-T. Nguyen, S. Y. Tee, C. Y. J. Lim, X. Y. Tan, M.-F. Ng, J. Xu, Z. W. Seh, *Nano Lett.* **2021**, *21*, 5401.
[68] Q. Guo, S. Sun, K. Kim, H. Zhang, X. Liu, C. Yan, H. Xia, *Carbon Energy* **2021**, *3*, 440.
[69] L. Hu, Y. Lu, T. Zhang, T. Huang, Y. Zhu, Y. Qian, *ACS Appl. Mater. Interfaces* **2017**, *9*, 13813.

[70] J. W. Jeon, D.-M. Kim, J. Lee, M. S. Kim, M. H. Jeon, R. Malpass-Evans, N. B. McKeown, K. T. Lee, B. G. Kim, *J. Power Sources* **2021**, *513*, 230539.
[71] C. Y. J. Lim, A. Y. S. Eng, A. D. Handoko, R. Horia, Z. W. Seh, *Nano Lett.* **2021**, *21*, 10538.
[72] Y. Liu, X. Li, Y. Sun, R. Yang, Y. Lee, J.-H. Ahn, *J. Alloys Compd.* **2021**, *853*, 157316.
[73] S. Ma, P. Zuo, H. Zhang, Z. Yu, C. Cui, M. He, G. Yin, *Chem. Commun.* **2019**, *55*, 5267.
[74] J. Mou, T. Liu, Y. Li, W. Zhang, M. Li, Y. Xu, J. Huang, M. Liu, *J. Mater. Chem. A* **2020**, *8*, 24590.
[75] D. Zhou, Y. Chen, B. Li, H. Fan, F. Cheng, D. Shanmukaraj, T. Rojo, M. Armand, G. Wang, *Angew. Chem., Int. Ed.* **2018**, *57*, 10168.
[76] A. Ghosh, S. Shukla, M. Monisha, A. Kumar, B. Lochab, S. Mitra, *ACS Energy Lett.* **2017**, *2*, 2478.
[77] T. W. Surta, E. Koh, Z. Li, D. B. Fast, X. Ji, P. A. Greaney, M. R. Dolgos, *Adv. Energy Mater.* **2022**, 2200647.
[78] L. Zhao, Z. Hu, W. Lai, Y. Tao, J. Peng, Z. Miao, Y. Wang, S. Chou, H. Liu, S. Dou, *Adv. Energy Mater.* **2021**, *11*, 2002704.
[79] A. Vasileiadis, Y. Li, Y. Lu, Y.-S. Hu, M. Wagemaker, *ACS Appl. Energy Mater.* **2022**, *6*, 127.
[80] Y. Li, A. Vasileiadis, Q. Zhou, Y. Lu, Q. Meng, Y. Li, P. Ombrini, J. Zhao, Z. Chen, Y. Niu, *Nat. Energy* **2024**, *9*, 134.
[81] S. Zhang, Y. Yao, Y. Yu, *ACS Energy Lett.* **2021**, *6*, 529.
[82] J. P. Perdew, K. Burke, M. Ernzerhof, *Phys. Rev. Lett.* **1996**, *77*, 3865.
[83] G. Kresse, J. Furthmüller, *Comput. Mater. Sci.* **1996**, *6*, 15.
[84] P. E. Blöchl, *Phys. Rev. B* **1994**, *50*, 17953.
[85] S. Grimme, J. Antony, S. Ehrlich, H. Krieg, *J. Chem. Phys.* **2010**, 132.
[86] S. Nosé, *J. Chem. Phys.* **1984**, *81*, 511.
[87] W. G. Hoover, *Phys. Rev. A* **1985**, *31*, 1695.
[88] A. Van der Ven, M. K. Aydinol, G. Ceder, G. Kresse, J. Hafner, *Phys. Rev. B* **1998**, *58*, 2975.
[89] A. S. Dalton, A. A. Belak, A. Van der Ven, *Chem. Mater.* **2012**, *24*, 1568.